Journal of Materials Chemistry A

ROYAL SOCIETY OF CHEMISTRY

PAPER

View Article Online
View Journal | View Issue

Cite this: J. Mater. Chem. A, 2023, 11, 26481

Copper hydroxide/basic copper salt derived Cu^0 with a clear grain boundary for selective electrocatalytic CO_2 reduction to produce multicarbon products†

Shuchang Song,‡[a] Haoyang Wu,‡[a] Benqiang Tian,[a] Ying Zhang, *[b] Yun Kuang*[ac] and Xiaoming Sun [a]

Electrocatalytic CO_2 reduction (ECR) is one of the most promising ways to mitigate CO_2 and fuel production, and multicarbon products (C_{2+}) with high chemical value attract lots of interest. Cu is a unique electrocatalyst that can convert CO_2 to multicarbon products, but with limited selectivity and activity. Here, aiming for a clear Cu^0 nanoparticle structure with a clear grain boundary, we report a simple and effective method of $Cu(OH)_2$/basic copper sulphate compound material synthesis, which is *in situ* reduced to Cu^0 nanoparticles with a clear grain boundary (GB) during the ECR process. The $Cu(OH)_2$/basic copper sulphate-derived Cu nanoparticles show a high C_{2+} faradaic efficiency (FE) of 81% at −1.2 V *vs.* RHE, which surpasses that of state-of-the-art Cu-based catalysts evaluated in an H-type cell. Extending the method to other basic copper salts (BCS), we successfully synthesized three other $Cu(OH)_2$/BCS species (nitrate, carbonate and chloride), which were also converted to Cu^0 with a clear grain boundary during ECR. DFT calculation results reveal that the GB sites could effectively decrease the energy barrier of the reactant CO_2 adsorption and critical C–C coupling steps, which endows the derived Cu electrocatalyst with high selectivity for C_2H_4 and C_{2+} products.

Received 17th September 2023
Accepted 16th November 2023

DOI: 10.1039/d3ta05628g

rsc.li/materials-a

Introduction

Following increased development of science and technology, increasing emission of the greenhouse gas CO_2 has caused a series of environmental problems.[1] In satisfying the demand for large amounts of industrial production, the substantial consumption of fossil fuels exacerbates the difficulty in abating the conflict between energy requirements and the environment.[2,3] Electrocatalytic CO_2 reduction (ECR) is a promising method to convert CO_2, driven by intermittent renewable electricity under mild temperature and ambient pressure. The products formed include CO, CH_4, C_2H_4, HCOOH, C_2H_5OH, and C_3H_7OH.[4] Among these products, CO and HCOOH, obtained during the ECR process by 2 electron transfer, are relatively promising, and their faradaic efficiency could even reach close to 100%.[5–7] Multicarbon products, such as C_2H_4, C_2H_5OH and C_3H_7OH, attract more attention because of their higher energy density and chemical value.[8,9] However, the formation of multicarbon products (C_{2+}) has always been coupled with multi-electron transfer, intricate reaction pathways and high reaction barriers, which impedes systematic research and further practical applications.[10]

The cathodic catalyst is a primary factor in ECR performance. Among metals, Cu is unique, and can catalyze the reaction of CO_2 to form multi-electron products and multicarbon products, but unfortunately with a relatively low selectivity and activity.[11] Consequently, modified Cu based catalysts have been broadly researched, including studies of particle size and morphology manipulation, tandem catalysis, valence regulation, grain boundary construction, *etc.*[12–15] Previous research has found that the constructed grain boundary of Cu is a key reason for enhanced ECR performance towards C_{2+} products.[16,17] However, the assessment of factors of enhanced ECR performance in many reported Cu catalysts with grain boundaries is often disrupted by other parameters, such as different support materials and dynamic intermediate valence states of Cu,[18,19] which have also proved to have an impact on the ECR performance of Cu catalysts.[20–22] Hence, further attempts are needed to construct a stable Cu^0 grain boundary

[a]State Key Laboratory of Chemical Resource Engineering, College of Chemistry, Beijing University of Chemical Technology, Beijing 100029, P. R. China. E-mail: kuangy@tsinghua-sz.org

[b]Key Laboratory of Synthetic and Biological Colloids, Ministry of Education, School of Chemical and Material Engineering, Jiangnan University, Wuxi 214122, China. E-mail: ying.zhang@jiangnan.edu.cn

[c]Ocean Hydrogen Energy R&D Center, Research Institute of Tsinghua University, Shenzhen 518057, P. R. China

† Electronic supplementary information (ESI) available. See DOI: https://doi.org/10.1039/d3ta05628g

‡ These authors contributed equally to this work.

via precursors with clear structures in order to gain greater insight into the functionality of the Cu^0 grain boundary for high selectivity of C_{2+} production without possible underlying disturbance.

Herein, in an effort to achieve a large amount of clear Cu grain boundary, we successfully designed and synthesized copper hydroxide/basic copper sulphate (denoted as $Cu(OH)_2$/BCS-S) composite materials by a simple and effective hydrothermal method. We found that the $Cu(OH)_2$/BCS-S was *in situ* reduced to Cu^0 with a clear grain boundary during the ECR process, which could effectively convert CO_2 into C_{2+} products and achieve impressive C_2H_4 and C_{2+} faradaic efficiencies of 65% and 81% at −1.2 V *vs.* RHE. DFT calculation indicates easier CO_2 reactant adsorption and a reduced energy barrier of C–C coupling on grain boundary sites, where the C–C coupling is considered to be a key energy demanding path towards C_{2+} products. Based on this result, we then successfully synthesized three other $Cu(OH)_2$/BCS species: $Cu(OH)_2$/basic copper nitrate, $Cu(OH)_2$/basic copper carbonate and $Cu(OH)_2$/basic copper chloride (denoted as $Cu(OH)_2$/BCS-N, $Cu(OH)_2$/BCS-Car and $Cu(OH)_2$/BCS-Ch, respectively). The results show that these compound materials were all reduced to Cu^0 nanoparticles with clear grain boundaries and, as a result, also achieved comparable faradaic efficiencies of C_2H_4 and C_{2+} products.

Results and discussion

The synthesis of $Cu(OH)_2$/BCS-S is achieved by means of alkalization of BCS-S. We first assessed the impact of the alkalization of BCS-S using X-ray diffraction (XRD), and the morphology using scanning electron microscopy (SEM). With an increase of the applied amount of alkali, the crystalline phase was gradually converted from pure basic copper sulphate to $Cu(OH)_2$/BCS-S compound materials (7 mmol NaOH), then to pure $Cu(OH)_2$ (more than 8 mmol NaOH) (Fig. 1a). It is worth noting that it requires an accurate amount of NaOH (7 mmol) for the successful synthesis of the $Cu(OH)_2$/BCS-S compound materials. The process of gradual alkalization of BCS-S also has an impact on the morphology, which varies from original nanosheets with a diameter of 200–500 nm to nanowires with a length of 0.5–2 μm (Fig. S1 and S2†).

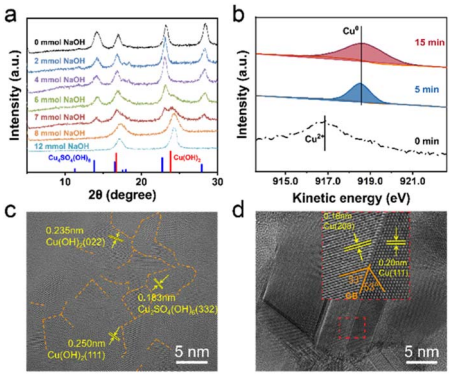

Fig. 1 Structure and characterization of Cu-gas catalysts. (a) XRD pattern of BCS manipulated with an increased amount of alkali. (b) Dynamic Cu valence analysis using the *in situ* Cu LMM energy spectrum of Cu(OH)2/BCS-S. (c) Spherical aberration corrected transmission electron microscopy (AC-TEM) analysis of $Cu(OH)_2$/BCS-S before reduction. The different crystalline regions are separated by yellow dashed lines for clear observation. (d) AC-TEM analysis of $Cu(OH)_2$/BCS-S-derived Cu with the part in the red dashed box showing the finer structure of the grain boundary (GB) formed after reduction. All of the electroreduction processes were carried out at −1.2 V *vs.* RHE in 1 M KI saturated with CO_2 under ambient temperature and pressure.

Owing to the sensitivity of Cu species to O_2 in the air when the reducing potential is applied, *in situ* characterizations are essential for probing the active species and dynamic evolution of Cu-based catalysts during ECR. Here, *in situ* X-ray photoelectron spectroscopy (XPS) analysis was used to obtain qualitative information on the Cu valence (Fig. 1b, S3 and S4†). The *in situ* Cu LMM and 2p spectra show that the valence of Cu species in the $Cu(OH)_2$/BCS-S was reduced from +2 to 0 within the first 5 minutes at −1.2 V *vs.* RHE, and the Cu^0 of 0 valence remained invariant after the first 5 minutes. This phenomenon is common for many copper oxide species, as the practical electrochemical environment during ECR is strongly reductive.[23–25] In addition, we used the XRD of $Cu(OH)_2$/BCS-S at different reduction times at −1.2 V *vs.* RHE to quantitatively analyze the crystalline phases and valence states of the Cu species (Fig. S5†). The results show that the $Cu(OH)_2$/BCS-S was completely transformed to Cu^0 species within the first 5 minutes, and remained stable after 1 hour, which agrees well with the *in situ* XPS analysis.

Subsequently, we applied spherical aberration corrected transmission electron microscopy (AC-TEM) to gain greater insight into the fine structure evolution of $Cu(OH)_2$/BCS-S nanowires during ECR, and the results show that there are many crystalline regions before reduction, which belong to different crystal facets of the $Cu(OH)_2$ and BCS-S species (Fig. 1c). After the $Cu(OH)_2$/BCS-S nanowires were reduced for 5 minutes at −1.2 V *vs.* RHE during ECR, the $Cu(OH)_2$/BCS-S with a nanowire morphology became Cu nanoribbons with large amounts of clear grain boundaries (Fig. 1d and S6†). These are assembled from different Cu facets with prominent angles between the facets. The clear grain boundary was proved to supply a number of active sites for the ECR process, and is beneficial to the kinetics of CO dimerization.[26–28]

For the measurement of the ECR performance of the as-synthesized materials discussed above, an H-type cell with two compartments was applied, and KI was used as a catholyte to promote charge transfer and improve selectivity to C_{2+} products by specific adsorption on the Cu surface.[29–31] We first measured the ECR performance of BCS-S manipulated with different amounts of alkali (Fig. S7†). The Cu derived from these materials all shows low competing hydrogen evolution reaction (HER) selectivity and the ECR products are mainly C_2H_4. When the amount of alkali is increased, the faradaic efficiency of C_2H_4 first increases and then decreases, and when the amount of alkali was 7 mmol, the Cu ($Cu(OH)_2$/BCS-S-derived Cu) delivered peak faradaic efficiencies of C_2H_4 and C_{2+} of 65% and 85%. This result could be a good indication that only when BCS-S and $Cu(OH)_2$ phases recombined adequately could the Cu derived

from them with a clear grain boundary achieve a great improvement of selectivity towards C_2H_4 and C_{2+} products.

We then evaluated more comprehensive ECR performance of $Cu(OH)_2$/BCS-S-derived Cu. By comparing linear sweep voltammetry (LSV) activity in 1 M KI saturated with N_2 and CO_2 (Fig. 2a), we can see a lower onset potential as well as a higher current density under a CO_2 atmosphere, which indicates a higher electrocatalytic activity towards ECR compared to HER. Subsequently, we explored some test parameters, such as catalyst loading, Nafion dosage and catholytes, to figure out the optimized layout (Fig. S8†). Fig. 2b shows the cathodic product distribution at different overpotentials, and when the overpotential is increased, the main product changes from CO to C_2H_4 (as high as 65%), then to H_2. The catalytic behavior here is common because C_2H_4 production is a CO demanding process, where CO is consumed in large amounts to accomplish the C–C coupling step, and on the other hand, large overpotentials will lead to accelerated HER kinetics.[32–34] As for the selectivity for C_2H_4 and C_{2+} products, Fig. 2c shows that the $Cu(OH)_2$/BCS-S-derived Cu could deliver an impressive faradaic efficiency of C_2H_4 and C_{2+} of 65% and 81%, respectively, at −1.2 V *vs.* RHE with a total current density of 30.2 mA cm^{-2}. Moreover, the stability test indicates good stability after continuous cathodic polarization for 7 hours, where the current density is basically steady and the faradaic efficiency of C_2H_4 is also maintained at more than 58.2% (Fig. 2d).

To stress the vital importance of the grain boundary in $Cu(OH)_2$/BCS-S-derived Cu for high activity and selectivity of C_{2+} products, we comprehensively compared again the ECR performance of $Cu(OH)_2$/BCS-S-derived Cu, BCS-S-derived Cu and $Cu(OH)_2$-S-derived Cu, where the $Cu(OH)_2$-S was evolved from BCS-S manipulated with excess alkali. These Cu based catalysts with +2 valence of Cu will be easily reduced to Cu^0, according to many reports.[24,25,35] Similarly, the overpotential-dependent product distributions of BCS-S-derived Cu and $Cu(OH)_2$-S-derived Cu show peak faradaic efficiencies of C_2H_4 of 42% and 46%, which are far lower than that of $Cu(OH)_2$/BCS-S-derived Cu (65%) (Fig. S9 and S10†). Also, LSV in 1 M KI saturated with CO_2 shows a higher current activity towards ECR for $Cu(OH)_2$/BCS-S-derived Cu. Furthermore, electrochemical impedance spectroscopy (EIS) was employed to obtain further information on the difference in electrochemical behavior of the three catalysts (Fig. S11†). The Nyquist plots of $Cu(OH)_2$/BCS-S-derived Cu show a smaller hoop, which demonstrates a lower faradaic impedance as well as faster kinetics of charge transfer. These results coincide well with the enhanced activity and selectivity of $Cu(OH)_2$/BCS-S-derived Cu towards C_{2+} products compared to BCS-S-derived Cu and $Cu(OH)_2$-S-derived Cu. In general, the diverse electrochemical behavior of the three catalysts shows the importance of the grain boundary in $Cu(OH)_2$/BCS-S-derived Cu to promote C_{2+} production during ECR.

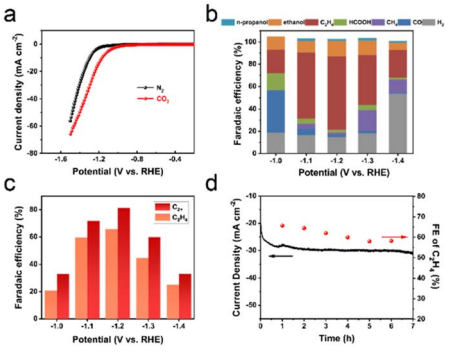

Fig. 2 ECR performance of $Cu(OH)_2$/BCS-S-derived Cu. (a) Linear sweep voltammetry (LSV) of $Cu(OH)_2$/BCS-S-derived Cu in 1 M KI catholyte saturated with N_2 or CO_2 at a scan rate of 5 mV s^{-1}. (b) Cathodic product distribution at different potentials after an hour of the ECR. (c) Faradaic efficiency of C_2H_4 and C_{2+} at different potentials after an hour of ECR. (d) The stability test at −1.2 V *vs.* RHE. The layout of all the ECR performance tests involves 1 M KI catholyte saturated with CO_2 under ambient temperature and pressure.

To gain further insight into the mechanism by which the Cu grain boundary in $Cu(OH)_2$/BCS-S-derived Cu leads to high selectivity of C_{2+} production, DFT calculations were employed. The stable atomic structure of the Σ3 twin boundary model was applied here as it represents the highest density of coincident lattice sites at the GB plane, which includes convex grain boundary sites (GB1) and concave grain boundary sites (GB2) (Fig. 3a).[17,36] We first compared the adsorption energy of the CO_2 reactant on GB1, GB2 and Cu(111), where Cu(111) was chosen for comparison as it is the main contributor to the facets in the Cu nanoparticles according to the XRD results shown above (Fig. 3b). The results reveal that compared to the weak adsorption of CO_2 on Cu(111) sites, the adsorption energy of CO_2 decreased dramatically, even to negative values, on GB1 and GB2, which greatly promotes reactant adsorption on GB1 and GB2 and thus could promote the CO_2 reduction process.[37]

In addition, Gong and coworkers recently proposed and validated a possible rate limiting step for 2 e^- product (CO and HCOOH) production, and found that the adsorption of CO_2 should be the rate limiting step,[38] thus the promoted adsorption of CO_2 here is proposed to facilitate the production of the key intermediate *CO, which is in great demand for C–C coupling to form C_{2+} products. On the other hand, as HER seems to be an inevitable accompanying process in aqueous ECR, improved adsorption action of the CO_2 reactant on the grain boundary could suppress the competing HER to some extent due to the site blocking effects.

Most mechanistic understanding of the reaction pathway of C_{2+} production agrees that C–C coupling is an essential step to produce multi-carbon products.[39,40] The surface coverage of *CO should be much larger than that of *CHO or *COH, as CO is one of the major products in ECR, which indicates that direct *CO dimerization is more likely to occur than C–C coupling by *CO and *CHO (or *COH).[41] Additionally, a large number of studies indicate that the C–C coupling step forms a combination of two adsorbed CO species, and is also the rate limiting step,[19,42,43] therefore the energy barrier of *COCO formation is an appropriate descriptor to embody the critical C–C coupling step. According to our calculation, Fig. 3c illustrates that the energy barrier of *CO–CO formation decreased a lot on GB1 and GB2, which proves that a C–C coupling process was promoted for C_{2+} production when the grain boundary was present as active sites.

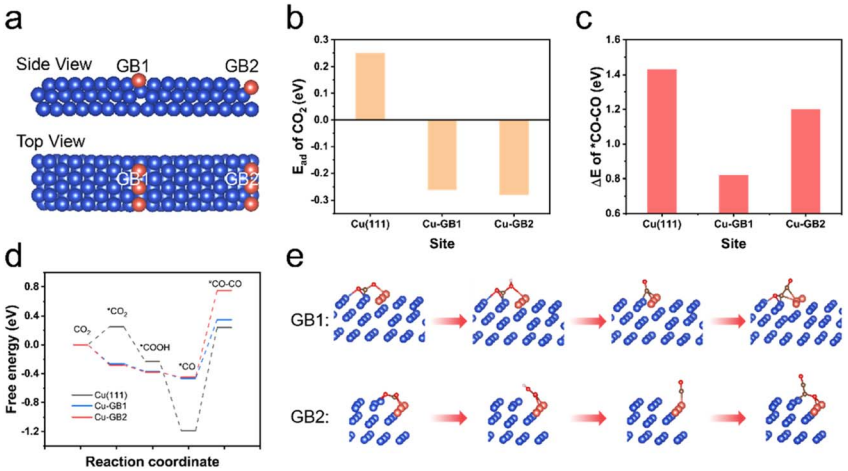

Fig. 3 DFT calculation of the Cu grain boundary. (a) Side and top view of two types of constructed Cu grain boundary: convex grain boundary sites (GB1) and concave grain boundary sites (GB2), which are shown by the light brown color. (b) Calculated adsorption of CO_2 on GB1, GB2 and Cu(111) facets. (c) Calculated energy barriers for the coupling of adsorbed CO on GB1, GB2 and Cu(111) facets. (d) Free energy of different adsorbed intermediates during CO_2 reduction to form *COCO on GB1, GB2 and Cu(111). (e) The evolution of the optimized adsorption structures for each reaction coordinate on GB1 and GB2.

As for the overall reaction coordinate of CO_2 reduction to form the critical *CO–CO intermediate, according to a large number of previous reports,[44,45] we adapted the reaction pathway as follows:

$$CO_2(g) + * \rightarrow *CO_2 \quad (1)$$

$$*CO_2 + H^+ + e^- \rightarrow *COOH \quad (2)$$

$$*COOH + H^+ + e^- \rightarrow *CO \quad (3)$$

$$2*CO \rightarrow *COCO \quad (4)$$

The free energies of each reaction coordinate are presented in Fig. 3d. We noticed that C–C coupling is a highly energy demanding step, which is however promoted a lot on grain boundary sites compared to Cu(111) sites. The dynamic optimized structure evolution of the involved reaction coordinates on the grain boundary and Cu(111) is shown in Fig. 3e and S12.† In summary, our calculation results suggest that compared to Cu(111) sites, the grain boundary sites here could promote CO_2 reactant adsorption, and are beneficial for the production of the key intermediate *CO, which is needed to satisfy the consumption requirements of the C–C coupling step. A decreased energy barrier for the critical C–C coupling step on grain boundary sites helps further to form desired C_{2+} products. The calculation results agree well with the high selectivity of C_{2+} products catalyzed by $Cu(OH)_2$/BCS-S-derived Cu with a clear grain boundary.

To explore the universality of the *in situ* construction of grain boundaries in $Cu(OH)_2$/BCS-S-derived Cu, we extended the method to other basic copper salts (nitrite, carbonate and chloride). Similarly, by gradual alkalization of three BCS precursors (Fig. S13–S15†), we found that the crystalline phase evolved from the pure BCS phase to $Cu(OH)_2$/BCS compound materials, then to the pure $Cu(OH)_2$ phase, where the optimal NaOH amounts required for the synthesis of $Cu(OH)_2$/BCS-N, $Cu(OH)_2$/BCS-Car and $Cu(OH)_2$/BCS-Ch compound materials are 1 mmol, 5 mmol and 1 mmol, respectively.

The difference between the four $Cu(OH)_2$/BCS compound materials lies first in their morphologies (Fig. S16†), which include nanowires for $Cu(OH)_2$/BCS-S, nanowire assembled nanoparticles for $Cu(OH)_2$/BCS-N, long and straight nanowires for $Cu(OH)_2$/BCS-Car, and randomly oriented nanowires for $Cu(OH)_2$/BCS-Ch. To explore whether the *in situ* construction of grain boundaries is universal for the four $Cu(OH)_2$/BCS species, the four catalysts were cathodic polarized for 5 minutes, and the resulting fine structures are shown in Fig. 4a, which indicates the clear grain boundaries in the four $Cu(OH)_2$/BCS-derived Cu species. The results proved well the universality of *in situ* grain boundary construction from $Cu(OH)_2$/BCS compound materials. Moreover, we further analysed the specific construction of the as-formed Cu^0 grain boundary in the $Cu(OH)_2$/BCS-derived Cu, which shows the typical Cu [n(200) × (111)] step sites (Fig. S20†). Owing to the specific edge defect structure, it's widely believed that the grain boundary (Cu [n(200) × (111)] step sites) is preponderant for facilitating the key C–C coupling process, thus leading to promoted C_{2+} product formation.[46,47]

The ECR performances of the $Cu(OH)_2$/BCS-N-derived Cu, $Cu(OH)_2$/BCS-Car-derived Cu and $Cu(OH)_2$/BCS-Ch-derived Cu are similar to that of the $Cu(OH)_2$/BCS-S-derived Cu (Fig. S17–S19†), for which the major product is also C_2H_4. Only when the amount of alkali used to form $Cu(OH)_2$/BCS compound materials was moderate was the resulting ECR performance towards C_2H_4 products improved to 62.5%, 63.2% and 65.6% for $Cu(OH)_2$/BCS-N-derived Cu (at −1.3 V *vs.* RHE), $Cu(OH)_2$/BCS-Car-derived Cu (at −1.3 V *vs.* RHE) and $Cu(OH)_2$/BCS-Ch-derived Cu (at −1.2 V *vs.* RHE), respectively. By comparison, the three Cu species derived from the BCS precursors (BCS-N, BCS-Car and BCS-Ch) show relatively low C_2H_4 faradaic efficiencies of 46.2%, 33.5% and 30.4%, respectively. The Cu

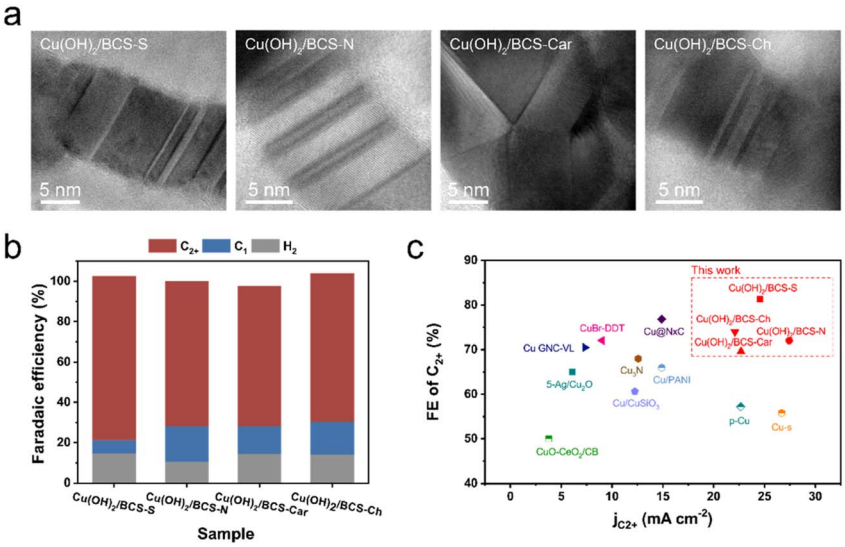

Fig. 4 The grain boundaries in the four $Cu(OH)_2$/BCS-derived Cu species and their corresponding ECR performance towards C_{2+} products. (a) AC-TEM for the *in situ* constructed grain boundaries in the four $Cu(OH)_2$/BCS-derived Cu species, which are formed after *in situ* ECR for 5 minutes. (b) The faradaic efficiency of C_{2+}, C_1 and H_2 of the four $Cu(OH)_2$/BCS-derived Cu species after an hour of ECR at their optimal potentials. (c) Comparison of the selectivity and activity for C_{2+} products exhibited by our catalysts with some other Cu based catalysts previously reported.

derived from the $Cu(OH)_2$ ($Cu(OH)_2$ is formed by using excess alkali with BCS-N, BCS-Car and BCS-Ch) also shows relatively low C_2H_4 faradaic efficiencies of 48.2%, 48.9% and 49.2%, respectively. Similar to $Cu(OH)_2$/BCS-S, these comparative results stress again the critical impact of the grain boundaries in $Cu(OH)_2$/BCS-derived Cu on the improved selectivity towards C_2H_4 production.

As for the desired C_{2+} products of the four $Cu(OH)_2$/BCS-derived Cu, Fig. 4b shows that the optimal C_{2+} product selectivities could reach as high as 81.3%, 72%, 69.6% and 73.9% (with suppressed low selectivities for H_2 of 6.7%, 17.6%, 13.7% and 16.1%) for $Cu(OH)_2$/BCS-S-derived Cu, $Cu(OH)_2$/BCS-N-derived Cu, $Cu(OH)_2$/BCS-Car-derived Cu and $Cu(OH)_2$/BCS-Ch-derived Cu, respectively. The slight difference in the ECR performance for $Cu(OH)_2$/BCS-S derived Cu may be because of the greater uniformity of its compound precursors. Compared with the other BCS species, a larger ionic radius of the sulfate radical leads to a lower hydration enthalpy and solubility of BCS-S,[48] which may result in a greater uniformity of $Cu(OH)_2$/BCS-S during the gradual conversion of BCS-S to $Cu(OH)_2$, as well as more grain boundary formation during the reduction of $Cu(OH)_2$/BCS-S to Cu^0. According to our analysis, the superb ECR performance towards C_{2+} production comes from *in situ* constructed grain boundaries to a great extent, and to the best of our knowledge, this performance is better than that of state-of-the-art Cu-based catalysts evaluated in H-type cells as Fig. 4c and Table S2† show.

Conclusion

In summary, we have successfully synthesized $Cu(OH)_2$/BCS-S compound materials by gradually applying alkali to the BCS-S precursor. The synthesized $Cu(OH)_2$/BCS-S is *in situ* reduced to a clear Cu^0 nanoparticle structure, with clear grain boundaries, which exhibited excellent ECR performance for C_2H_4 and C_{2+} production. The peak faradaic efficiencies of C_2H_4 and C_{2+} on the $Cu(OH)_2$/BCS-S-derived Cu could reach 65% and 81%, respectively, with a current density of 30.2 mA cm^{-2}. This performance exceeds that of state-of-the-art catalysts evaluated in an H-type cell. Upon extension to three other BCS species (BCS-N, BCS-Car and BCS-Ch), we successfully synthesized three other $Cu(OH)_2$/BCS compounds, and observed again the *in situ* formation of three $Cu(OH)_2$/BCS-derived Cu^0 species with clear grain boundaries, which also delivered high faradaic efficiencies of C_2H_4 and C_{2+} products (62.5% and 72% for $Cu(OH)_2$/BCS-N-derived Cu; 63.2% and 69.6% for $Cu(OH)_2$/BCS-Car-derived Cu; 65.6% and 73.9% for $Cu(OH)_2$/BCS-Ch-derived Cu). DFT calculation revealed a lower energy demand for initial CO_2 adsorption and the coupling of two *CO species on grain boundary sites, which enabled the promoted formation of key *CO intermediates and facilitated C–C coupling towards C_{2+} formation, respectively. Our research presents a novel and simple method for a large amount of clear grain boundary construction and promoted ECR performance for C_2H_4 and C_{2+} production.

Author contributions

Shuchang Song performed the material synthesis, characterization and electrochemical measurements. Haoyang Wu and Benqiang Tian analyzed the data and wrote the manuscript. Ying Zhang conducted the manuscript review and editing. Xiaoming Sun and Yun Kuang proposed the research direction and guided the whole experiment. All authors have given approval to the final version of the manuscript.

Conflicts of interest

There are no conflicts of interest to declare.

Acknowledgements

This work was supported by National Key Research and Development Program of China (No. 2022YFC2105900), National Key Research and Development Project (2018YFB1502401 and 2018YFA0702002), the Program for Changjiang Scholars and Innovation Research Team in the University (IRT1205), National Natural Science Foundation of China (22379054), the Fundamental Research Funds for the Central Universities and China Scholarship Council. We thank Prof. Zhi-jian Zhao for his help in DFT calculation.

References

1 S. J. Davis, K. Caldeira and H. D. Matthews, *Science*, 2010, **329**, 1330–1333.
2 O. Levitan, J. Dinamarca, G. Hochman and P. G. Falkowski, *Trends Biotechnol.*, 2014, **32**, 117–124.
3 G. P. Peters, J. C. Minx, C. L. Weber and O. Edenhofer, *Proc. Natl. Acad. Sci. U.S.A.*, 2011, **108**, 8903–8908.
4 Y. Y. Birdja, E. Pérez-Gallent, M. C. Figueiredo, A. J. Göttle, F. Calle-Vallejo and M. T. M. Koper, *Nat. Energy*, 2019, **4**, 732–745.
5 H. M. Jhong, C. E. Tornow, B. Smid, A. A. Gewirth, S. M. Lyth and P. J. Kenis, *ChemSusChem*, 2017, **10**, 1094–1099.
6 Q. Hao, Q. Tang, H. X. Zhong, J. Z. Wang, D. X. Liu and X. B. Zhang, *Sci. Bull.*, 2022, **67**, 1477–1485.
7 M. Liang, Y. Liu, H. Huang, L. Diao, J. Mu, Z. Miao, J. Zhou and S. Zhuo, *Chem. Eng. J.*, 2022, 450.
8 J. M. Spurgeon and B. Kumar, *Energy Environ. Sci.*, 2018, **11**, 1536–1551.
9 S. Chu, Y. Cui and N. Liu, *Nat. Mater.*, 2016, **16**, 16–22.
10 S. Xu and E. A. Carter, *Chem. Rev.*, 2019, **119**, 6631–6669.
11 Z. Gu, H. Shen, L. Shang, X. Lv, L. Qian and G. Zheng, *Small Methods*, 2018, **2**, 1800121.
12 Y. Wang, X. Zheng and D. Wang, *Nano Res.*, 2021, **15**, 1730–1752.
13 Y. Zhu, X. Cui, H. Liu, Z. Guo, Y. Dang, Z. Fan, Z. Zhang and W. Hu, *Nano Res.*, 2021, **14**, 4471–4486.
14 S. Hong, H. G. Abbas, K. Jang, K. K. Patra, B. Kim, B. U. Choi, H. Song, K. S. Lee, P. P. Choi, S. Ringe and J. Oh, *Adv. Mater.*, 2022, **35**, 2208996.
15 C. W. Li, J. Ciston and M. W. Kanan, *Nature*, 2014, **508**, 504–507.
16 A. Verdaguer-Casadevall, C. W. Li, T. P. Johansson, S. B. Scott, J. T. McKeown, M. Kumar, I. E. Stephens, M. W. Kanan and I. Chorkendorff, *J. Am. Chem. Soc.*, 2015, **137**, 9808–9811.
17 Z. Chen, T. Wang, B. Liu, D. Cheng, C. Hu, G. Zhang, W. Zhu, H. Wang, Z. J. Zhao and J. Gong, *J. Am. Chem. Soc.*, 2020, **142**, 6878–6883.
18 X. Feng, K. Jiang, S. Fan and M. W. Kanan, *ACS Cent. Sci.*, 2016, **2**, 169–174.
19 X. Huang, D. Wang, S. Yan, P. An, J. Han, Z. Guo, X. Li, Z. Chen, L. Chang, S. Lu and Z. Tang, *Nano Res.*, 2022, **15**, 7910–7916.
20 Y. Wu, C. Chen, X. Yan, R. Wu, S. Liu, J. Ma, J. Zhang, Z. Liu, X. Xing, Z. Wu and B. Han, *Chem. Sci.*, 2022, **13**, 8388–8394.
21 Q. Fan, X. Zhang, X. Ge, L. Bai, D. He, Y. Qu, C. Kong, J. Bi, D. Ding, Y. Cao, X. Duan, J. Wang, J. Yang and Y. Wu, *Adv. Energy Mater.*, 2021, 11.
22 C. Guo, Y. Guo, Y. Shi, X. Lan, Y. Wang, Y. Yu and B. Zhang, *Angew. Chem., Int. Ed.*, 2022, **61**, e202205909.
23 L. C. Pardo Pérez, A. Arndt, S. Stojkovikj, I. Y. Ahmet, J. T. Arens, F. Dattila, R. Wendt, A. Guilherme Buzanich, M. Radtke, V. Davies, K. Höflich, E. Köhnen, P. Tockhorn, R. Golnak, J. Xiao, G. Schuck, M. Wollgarten, N. López and M. T. Mayer, *Adv. Energy Mater.*, 2021, 12.
24 Q. Lei, L. Huang, J. Yin, B. Davaasuren, Y. Yuan, X. Dong, Z. P. Wu, X. Wang, K. X. Yao, X. Lu and Y. Han, *Nat. Commun.*, 2022, **13**, 4857.
25 Y. Fu, Q. Xie, L. Wu and J. Luo, *Chin. J. Catal.*, 2022, **43**, 1066–1073.
26 C. Tang, Z. Chen, Y. Wang, T. Xiao, X. Li, C. Zheng, X. Xu and Z. Sun, *ACS Catal.*, 2022, **12**, 11838–11844.
27 C. Tang, J. J. Shi, X. W. Bai, A. Q. Hu, N. N. Xuan, Y. W. Yue, T. Ye, B. Liu, P. X. Li, P. Y. Zhuang, J. F. Shen, Y. Y. Liu and Z. Z. Sun, *ACS Catal.*, 2020, **10**, 2026–2032.
28 M. Jun, C. Kwak, S. Y. Lee, J. Joo, J. M. Kim, D. J. Im, M. K. Cho, H. Baik, Y. J. Hwang, H. Kim and K. Lee, *Small Methods*, 2022, **6**, e2200074.
29 D. Gao, F. Scholten and B. Roldan Cuenya, *ACS Catal.*, 2017, **7**, 5112–5120.
30 I. T. McCrum, S. A. Akhade and M. J. Janik, *Electrochim. Acta*, 2015, **173**, 302–309.
31 A. S. Varela, W. Ju, T. Reier and P. Strasser, *ACS Catal.*, 2016, **6**, 2136–2144.
32 J. Hou, X. Chang, J. Li, B. Xu and Q. Lu, *J. Am. Chem. Soc.*, 2022, **144**, 22202–22211.
33 M. Zhao, H. Tang, Q. Yang, Y. Gu, H. Zhu, S. Yan and Z. Zou, *ACS Appl. Mater. Interfaces*, 2020, **12**, 4565–4571.
34 A. R. Woldu, Z. Huang, P. Zhao, L. Hu and D. Astruc, *Coord. Chem. Rev.*, 2022, 454.
35 T. Moller, F. Scholten, T. N. Thanh, I. Sinev, J. Timoshenko, X. Wang, Z. Jovanov, M. Gliech, B. Roldan Cuenya, A. S. Varela and P. Strasser, *Angew. Chem., Int. Ed.*, 2020, **59**, 17974–17983.
36 K.-S. Kim, W. J. Kim, H.-K. Lim, E. K. Lee and H. Kim, *ACS Catal.*, 2016, **6**, 4443–4448.
37 L.-W. Chen, Y.-C. Hao, J. Li, L. Hu, Y. Guo, S. Li, D. Liu, Z. Zhu, S.-Q. Wu, H.-Z. Huang, A.-X. Yin, B. Wang and Y.-W. Zhang, *Sci. China Chem.*, 2022, **65**, 2188–2196.
38 W. Deng, P. Zhang, B. Seger and J. Gong, *Nat. Commun.*, 2022, **13**, 803.
39 J. D. Goodpaster, A. T. Bell and M. Head-Gordon, *J. Phys. Chem. Lett.*, 2016, **7**, 1471–1477.
40 K. Jiang, R. B. Sandberg, A. J. Akey, X. Liu, D. C. Bell, J. K. Nørskov, K. Chan and H. Wang, *Nat. Catal.*, 2018, **1**, 111–119.
41 T. K. Todorova, M. W. Schreiber and M. Fontecave, *ACS Catal.*, 2019, **10**, 1754–1768.
42 Y. Yan, Z. Zhao, J. Zhao, W. Tang, W. Huang and J.-M. Lee, *J. Mater. Chem. A*, 2021, **9**, 7496–7502.

43 D. Xiao, X. Bao, M. Zhang, Z. Li, Z. Wang, Y. Gao, Z. Zheng, P. Wang, H. Cheng, Y. Liu, Y. Dai and B. Huang, *Chem. Eng. J.*, 2023, 452.
44 J. Yu, J. Wang, Y. Ma, J. Zhou, Y. Wang, P. Lu, J. Yin, R. Ye, Z. Zhu and Z. Fan, *Adv. Funct. Mater.*, 2021, 31.
45 F. Hu, L. Yang, Y. Jiang, C. Duan, X. Wang, L. Zeng, X. Lv, D. Duan, Q. Liu, T. Kong, J. Jiang, R. Long and Y. Xiong, *Angew. Chem., Int. Ed.*, 2021, **60**, 26122–26127.
46 F. Yu, X. Liu, L. Liao, G. Xia and H. Wang, *Small*, 2023, **19**, e2301558.
47 Z. Gu, H. Shen, Z. Chen, Y. Yang, C. Yang, Y. Ji, Y. Wang, C. Zhu, J. Liu, J. Li, T.-K. Sham, X. Xu and G. Zheng, *Joule*, 2021, **5**, 429–440.
48 R. Mahmudov and C. P. Huang, *Sep. Purif. Technol.*, 2011, 77, 294–300.